Strain coupling and acoustic attenuation associated with glassy magnetic phase transitions in the disordered double perovskite La$_2$FeMnO$_6$

Dexin Yang,[1] Tao Yang,[1] Paromita Mukherjee,[2] Sian E. Dutton,[2] Dexuan Huo,[1] and Michael A. Carpenter[3]

[1]*College of Materials and Environmental Engineering, Hangzhou Dianzi University, Hangzhou 310018, China*
[2]*Cavendish Laboratory, University of Cambridge, Madingley Road, Cambridge CB3 0HE, England, United Kingdom*
[3]*Department of Earth Sciences, University of Cambridge, Downing Street, Cambridge CB2 3EQ, England, United Kingdom*

Elastic and anelastic anomalies in a ceramic sample of La$_2$FeMnO$_6$ have been characterized by resonant ultrasound spectroscopy in order to understand the strength and form of magnetoelastic coupling that accompanies the glassy magnetic transitions of a double perovskite with no long-range order of the B-site cations. The first transition, to a cluster glass below $\sim$280 K, does not appear to involve any significant coupling with strain. The second glassy transition, near 55 K, appears to conform to Vogel-Fulcher dynamics in which magnetic dissipation and acoustic loss peaks arise from freezing driven by interactions between ferromagnetic clusters, with an activation energy of $\sim$0.03 eV and time constant $\tau_o \sim 10^{-9}$ s. The magnetoelastic coupling mechanism appears to involve local spin states with strain relaxation enhanced by changes in local electronic structure. Mediation of the coupling via strain also ensures that local heterogeneity in the strain state, such as at ferroelastic twin walls, will contribute to the magnetic heterogeneity of these materials.

I. INTRODUCTION

The remarkable electronic and magnetic properties of double perovskites with B-site transition-metal ions, including room-temperature colossal magnetoresistance [1], high Curie temperature [2], half-metallic character [3], and multiferroicity [4], make them phases of topical interest in condensed-matter physics, materials physics, and materials science. Most of the functional properties develop when the two B-site ions are transition-metal elements, and this characteristic is probably due to the unpaired $3d$ electrons which strongly correlate with each other or with oxygen $2p$ electrons in the double perovskite structure [2,5]. In addition, charge transfer [6], low-temperature saturation magnetism [7], magnetodielectric properties [8], etc., are expected to be sensitive to the degree of B-site cation order. Because of the promising magnetoelectric, magnetodielectric, and colossal magnetoresistive properties, La$_2$BMnO$_6$, with $B =$ Ni, Co, Fe, etc., is highlighted among other members of the series. However, in comparison with La$_2$NiMnO$_6$ [8–22] and La$_2$CoMnO$_6$ [14,23–31], less attention has been paid to La$_2$FeMnO$_6$ (LFMO) even though ferromagnetic half-metallic properties were recently predicted by calculation [32]. Furthermore, bulk La$_2$NiMnO$_6$ and La$_2$CoMnO$_6$ are known as B-site ordered or partially ordered double perovskites [23,33,34], while bulk LFMO has complete B-site disorder [33].

It is well understood that octahedral tilting, ferroelectric displacements, cation ordering, and cooperative Jahn-Teller transitions in perovskites are typically accompanied by significant spontaneous strains that provide an indirect mechanism for coupling mechanisms between multiple order parameters. They are also a controlling factor in the dynamics and pinning of ferroelastic twin walls. Magnetoelastic effects are much more variable but are important in multiferroic systems [35].

LFMO provides an opportunity to investigate magnetoelastic coupling behavior in a glassy magnetic system where spin and orbital ordering effects are frustrated. The present paper follows from a study of the elastic and anelastic anomalies associated with coupled magnetic ordering and tilt transitions in Sr$_2$FeMoO$_6$, which displays variable degrees of cation order [7]. Resonant ultrasound spectroscopy (RUS) has been used to measure the elastic and anelastic response of a ceramic sample of LFMO displaying the frustrated magnetic responses associated with Fe/Mn disorder. Ac and dc magnetic susceptibilities have been used to characterize the glassy magnetic properties of the same sample.

II. CHARACTERISTIC STRUCTURE AND PROPERTIES OF LFMO

LFMO was reported by Jia *et al.* [36] to have a hexagonal perovskite structure at room temperature, but all subsequent determinations indicate that it is orthorhombic, in crystallographic space group *Pbnm* (conventional setting: *Pnma*) [37–45]. The equivalent structure with B-site ordering would be expected to have space group $P2_1/n$. Mn^{3+} is Jahn-Teller active while Fe^{3+} in its high spin state is not, so that substituting Fe^{3+} for Mn^{3+} is likely to reduce octahedral distortions. The inference from lattice parameters, at least, has been that cooperative Jahn-Teller effects are suppressed [46,47], though Palakkal *et al.* [45] found a small increase in octahedral site distortion between 300 and 100 K. Lowering of symmetry from cubic to orthorhombic is therefore due predominantly to octahedral tilting. The lack of free-energy drive for B-site ordering is due to Mn^{3+} and Fe^{3+} in its high spin state having the same radius, of $\sim$0.65 Å according to the tabulation of Shannon [48].

The magnetic state of LFMO at room temperature has been reported as being paramagnetic [36,38,42]. However, rather than having a discrete magnetic phase transition at low temperatures there are two spin freezing processes. The first is believed to be to a cluster glass [38,41,47] and the second to a ferromagneticlike structure [38,41,47]. This glassy freezing behavior is attributed to frustration arising from strong local competition in the disordered structure between Mn^{3+}-O-Mn^{3+} and Mn^{3+}-O-Fe^{3+} exchange interactions, which favor ferromagnetism, and Fe^{3+}-O-Fe^{3+} interactions, which favor antiferromagnetism [44,46,49].

Characteristic features of the dc magnetic properties are illustrated in Fig. 1 for the polycrystalline sample used in the present paper. First, there is a divergence of the magnetization, expressed as moment or susceptibility, between field cooled (FC) and zero-field cooled (ZFC) conditions at a temperature T_{irr} [Fig. 1(a)] [38,41,43,44,46,47], which decreases as the measuring field is increased [Fig. 1(a)] [44]. A rounded peak in the ZFC data occurs at a temperature, T_p, which is below T_{irr} [Fig. 1(a)] [38,41,43,44,46,47]. In the case of LFMO, this pattern has been taken to be indicative of the formation of a cluster glass [47]. Second, paramagnetism is indicated by a linear temperature dependence of the inverse susceptibility, χ^{-1}, at the highest temperature, corresponding to $\sim$350$-$400 K in this case [Fig. 1(b)] [41]. With falling temperature, values of χ^{-1} then dip below the Curie-Weiss line at a temperature T^* [$\sim$330 K in Fig. 1(b)] [41,43]. In a narrow temperature interval below T^*, the data can again be fit by a straight line and this has been interpreted in terms of a superparamagnetic state with preferred alignment of moments inside clusters and weak interactions between them [38,41]. However, an open hysteresis loop has been observed at $\sim$80 K [37,49], revealing the presence of a ferromagnetic component. Palakkal *et al.* [43] pointed out that the pattern of evolution of χ^{-1} in LFMO is comparable with that associated with the development of a Griffiths-like phase, i.e., ferromagnetic clusters in a paramagnetic host. According to Bhame *et al.* [49], the intermediate state could consist of a mixture of a ferromagnetic phase and a superparamagnetic phase, while Karpinsky *et al.* [46] discussed a model in which the two phases are ferromagnetic and antiferromagnetic. The rate of change of magnetization with temperature is greatest in the low-temperature region, as given by a broad minimum in the derivative dM/dT [43,44], and this is at $\sim$55 K in a 1000-Oe field for the sample used in the present paper [Fig. 1(c)]. Finally, ac susceptibility measurements have revealed a frequency dependence for the freezing process at these low temperatures (De *et al.* [41], and see below).

Within this broad pattern, there are many variations in the details of samples prepared for different studies. The open hysteresis loop at room temperature shown by de Lima *et al.* [47] indicates that the paramagnetic phase becomes stable only at higher temperatures in their sample, in the same way that it appears only to be stable down to $\sim$500 K in the sample of Palakkal *et al.* [43]. The divergence between FC and ZFC magnetization data has been reported as occurring at $\sim$260 K [38,41], $\sim$100 K [44], $\sim$150 K [46], and $\sim$60 K [47]. Not all samples show the dip of inverse susceptibility below the Curie-Weiss line with falling temperature [41,44]. The lowest temperature freezing process has been reported as
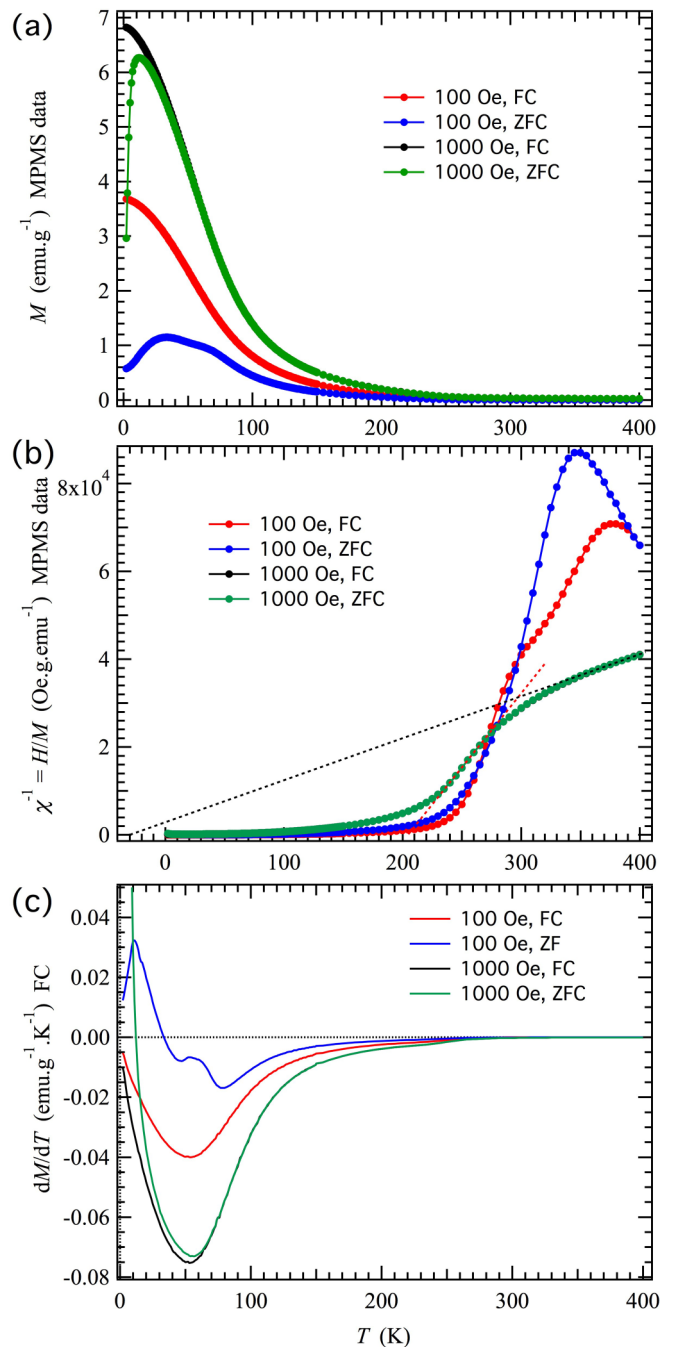
FIG. 1. (a) Thermal evolution of the zero-field cooled (ZFC) and field cooled (FC) magnetization, M, of a ceramic piece of LFMO with mass 0.0114 g at 100 and 1000 Oe under FC and ZFC conditions in a Quantum Design magnetic property measurement system (MPMS) instrument. (b) Temperature dependence of inverse susceptibility, χ^{-1}. The black dotted line is a fit to a 1000-Oe FC physical property measurement system above $\sim$330 K, which gives a Curie-Weiss temperature of -35 K. The red dotted line shows a linear fit to 1000-Oe FC MPMS data in the temperature interval 235–265, which gives a Curie-Weiss temperature of 205 K. (c) Derivative of magnetization with respect to temperature, dM/dT. The 100-Oe ZFC data have two minima, at $\sim$47 and $\sim$77 K. The 100-Oe FC data have a single minimum at $\sim$54 K. The 1000-Oe FC and ZFC data have single minima at $\sim$53 and $\sim$57 K, respectively.

occurring at $\sim$12 K [38], $\sim$20 K [41], and $\sim$65 K [47], but this also changes with changing field [41]. Another LFMO sample has been described as showing magnetic transitions at $\sim$60 and $\sim$425 K, with evidence of short-range ferromagnetic correlations extending up to $\sim$570 K [43]. Bhame *et al.* [49] suggested that one factor in this variability is the degree of local cation order but the samples prepared at different temperatures in their study also had different grain sizes. A further variable is oxygen content. Karpinsky *et al.* [46] reported that samples synthesized at high temperature in air have a slight oxygen excess, and that this results in slightly different magnetic properties in comparison with more nearly stoichiometric samples produced by annealing in vacuum. The expectation is also that both Fe and Mn have charge 3+, and this appears to be the case when it has been checked [36–38,43,49], with the exception that Palakkal *et al.* [45] produced a sample in which Fe^{2+}, Fe^{3+}, Mn^{3+}, and Mn^{4+} were detected. Their sample displayed a sharp change in electrical resistivity and a small anomaly in heat capacity at $\sim$135 K, which was explained as a transition to a low-temperature state in which the charges became localized.

III. EXPERIMENTAL METHODS

A. Sample preparation and characterization

A ceramic sample of LFMO was prepared by a conventional solid-state reaction method, using Reagent-grade La_2O_3 (Aladdin, AR), MnO_2 (Aladdin, AR), and Fe_2O_3 (Aladdin, AR) as starting materials. Stoichiometric amounts of these were mixed for about 6 h with ethanol in an agate ball mill. The powder mixtures were dried in an oven at 353 K for 12 h and then ground for about 30 min. The resulting homogeneous powder was calcined at 1372 K for about 50 h in air with an intermediate grinding stage. The final powder was pressed uniaxially at $\sim$25 MPa to produce a pellet with 10-mm diameter and $\sim$2-mm height which was heated in air at 1573 K for 6 h. This was sawn up so that different pieces could be used for different measurements. The piece used for RUS and dc magnetic measurements was a rectangular parallelepiped with dimensions $2.183 \times 1.758 \times 0.674$ mm^3 and mass 0.0114 g. The estimated density from these measurements is 4.41 g cm^{-3}, which is $\sim$70% of the theoretical density, 6.733 g cm^{-3}, calculated from unit-cell contents. The piece used for ac magnetic measurements had mass 0.0774 g.

Room-temperature x-ray-diffraction data were collected from a powdered piece of the fired ceramic pellet using an X'Pert Powder diffractometer (PANalytical) with CuK$_\alpha$ radiation. Collection conditions were: 5°–95° in two theta, 0.013° step size, 40.8 s/step. TOPAS-Academic V6 software [50] was used for Rietveld refinements to obtain the lattice parameters. The background and peak shapes were fit using a shifted Chebyshev function with eight parameters and a Pseudo-Voigt function (TCHZ type), respectively.

In order to characterize the surface morphology and check the stoichiometry of the sample, scanning electron microscopy (SEM) measurements were performed using an FEI Nova NanoSEM microscope with a Bruker Nano GmbH energy dispersive x-ray spectrometer (EDS) for elemental analysis. To obtain more precise data for the stoichiometric

ratio, the amounts of La, Fe, and Mn were determined using the inductively coupled plasma optical emission spectroscopy (ICP-OES) method (ICS-1100, Thermo Fisher). For this, a 3:1 mixture of HCl (37%) and HNO_3 (65%) was used to dissolve the sample.

B. Resistance

The resistance as a function of temperature was measured with a Quantum Design physical property measurement system (PPMS) using the standard four-probe technique.

C. Magnetic measurements

Dc magnetic measurements of moment as a function of temperature and as a function of field were carried out on the sample used for RUS (0.0114 g) using a Quantum Design PPMS DynaCool instrument in the temperature range 2–300 K. Additional measurements of dc moment up to 400 K were undertaken on the same sample using a Quantum Design MPMS3.

The ac susceptibility data reported here were obtained from the 0.0774-g piece of the original ceramic pellet using a Quantum Design magnetic property measurement system XL-7 superconducting quantum interference device magnetometer in the temperature interval 2–240 K. Ac measurements were also made on the PPMS instrument up to 300 K using the RUS sample. These gave comparable results, though with lower resolution due to the smaller mass.

D. Resonant ultrasound spectroscopy

The RUS method has been described in detail by Migliori *et al.* [51]. Low-temperature measurements presented here were obtained using Dynamic resonance system (DRS) "modulus II" electronics. The RUS sample holder was attached to the end of a stick inserted into an Orange helium-flow cryostat [52]. The parallelepiped was held across a pair of faces directly between two transducers during two automated sequences of data collection. In the first, the sample was cooled from $\sim$280 to $\sim$95 K in 5-K steps and then heated from $\sim$95 to $\sim$298 K in 2-K steps. The absolute uncertainty in temperature is believed to be less than $\pm$1 K, and temperature stability during data collection is believed to be better than $\pm$0.1 K. A settle time of 20 min before collecting a spectrum at each set point was introduced to allow for thermal equilibration, and each spectrum contained 65 000 data points in the frequency range 50–1200 kHz. The second data collection was a cooling sequence from $\sim$280 to $\sim$10 K in 30-K steps followed by heating from $\sim$10 to $\sim$305 K in 5-K steps, again with 20-min equilibration time at each set point.

Spectra were analyzed offline using the software package Igor Pro (WaveMetrics). An asymmetric Lorentzian function was used to fit individual resonance peaks to determine peak frequencies, f, and widths at half-maximum height, Δf. Each acoustic mode of the sample relies on some combination of elastic constants that scales with the square of its resonance frequency, f. The deformation involves primarily shearing rather than breathing motions so that, for a ceramic sample, f^2 values mainly depend on the shear modulus. Acoustic loss

(a)

(b)
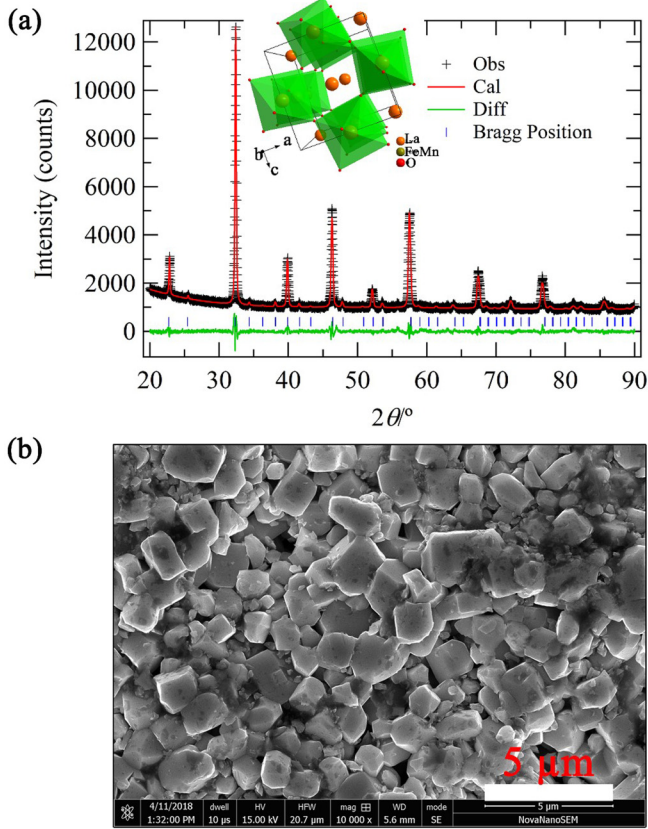
FIG. 2. (a) Room-temperature x-ray-diffraction pattern and fit from Rietveld refinement for LFMO. The observed profile is indicated by black crosses and the calculated profile is indicated by the red line. Bragg peak positions are shown by blue lines and the difference diffractogram (observed minus calculated) is shown in green. The inset shows the refined structure: green octahedra are Fe(Mn)O_6, Fe/Mn atoms are dark yellow, La atoms are orange, and O atoms are red. (b) A scanning electron micrograph of the LFMO surface microstructure.

can be expressed in terms of the inverse mechanical quality factor, Q^{-1}, which was taken as $\Delta f / f$.

IV. RESULTS

A. Structure, microstructure, and composition

The room-temperature diffraction pattern is shown in Fig. 2(a) and the inset shows the refined crystal structure ($R_{wp} = 5.842\%$, $R_p = 4.281\%$, and $\chi^2 = 1.896$). This is the expected orthorhombic perovskite structure in space group *Pnma* (no. 62), with two octahedral tilt systems and a disordered distribution of Fe and Mn on the B site. Values of the lattice parameters are $c < b/\sqrt{2} < a$ [$a = 5.5357$ (10) Å, $b = 7.8174$ (3) Å, $c = 5.5262$ (3) Å], consistent with suppression of cooperative Jahn-Teller distortions [46,47].

As shown in Fig. 2(b), the final LFMO sample consisted of a homogeneous distribution of crystals with shapes approximating that of a rectangular parallelepiped and dimensions in the range $\sim 0.5 - 2\,\mu$m. EDS confirmed the proportions of La, Fe, and Mn as La$_{2.23\pm0.038}$Fe$_{0.942\pm0.072}$Mn$_{1.043\pm0.071}$O$_6$. ICP-OES gave the atomic ratio of La:Fe:Mn more precisely
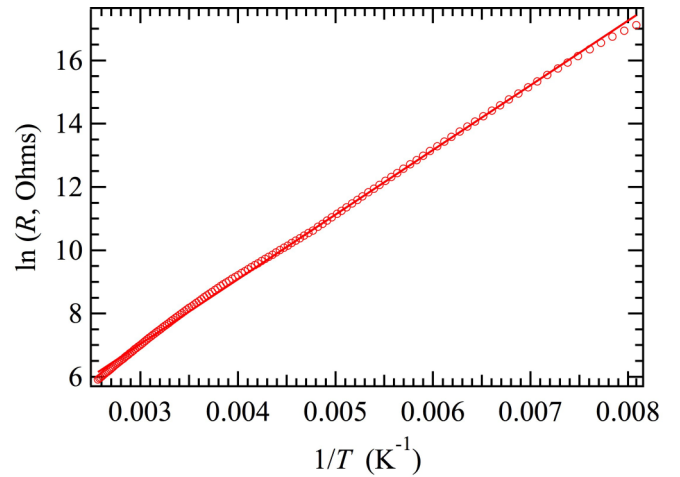
FIG. 3. Arrhenius plot of dc resistance as a function of temperature. The straight line fit to the data has slope 2044 ± 6 K.

as 2.09:0.96:1. Following the work of Karpinsky *et al.* [46], it seems likely that the sample contained a slight excess of oxygen in comparison with the ideal stoichiometry, which would be accounted for by a small proportion of vacancies on the cation sites.

B. Dc resistance

Data for dc resistance, R, measured in the temperature interval 124–390 K are consistent with an Arrhenius temperature dependence, $R = R_o \exp(E_a/T)$, as shown in Fig. 3. The straight line fit to the data gives a value for the activation energy, E_a, as 2044 ± 6 K (0.18 eV) and $R_o = 0.90 \pm 0.03\,\Omega$. This slope is essentially the same as shown for LFMO in a similar temperature interval by Li *et al.* [in their Fig. 6(i)] [44]. An equivalent plot to test the relationship for the small polaron hopping (SPH) model, $R/T = R_o \exp(E_a/T)$ [53], also gives a straight line with $E_a = 2261 \pm 8$ K (0.19 eV). There is no evidence in the data in Fig. 3 for the change in conduction mechanism reported at $\sim$135 K by Palakkal *et al.* [45]. Their value of the activation energy for the SPH model from measurements in the interval $\sim 135 - 300$ K was 0.14 eV.

C. Dc magnetism

The temperature dependence of zero-field cooled and field cooled dc magnetization, M, measured at 100 and 1000 Oe in the temperature range 2–400 K, was already shown in Fig. 1(a). The magnetization remains low from room temperature down to $\sim$250 K, where there is a smooth increase. Further steepening occurs below $\sim$100 K, followed by leveling off in the FC data or a rounded maximum in the ZFC data. The value of T_{irr} given by the temperatures at which the difference between FC and ZFC values reaches 1% is $\sim$43 K in a field of 1000 Oe. Values of T_p, the temperature at which there is a rounded maximum in the ZFC magnetization, are $\sim$34 K (100 Oe) and $\sim$12 K (1000 Oe).

Variations of χ^{-1} display similar trends below $\sim$270 K but some scatter at high temperatures [Fig. 1(b)]. The ZFC and FC data for 1000 Oe are self-consistent in having a linear trend at high temperatures, a change of slope at $T* \approx 330$ K,
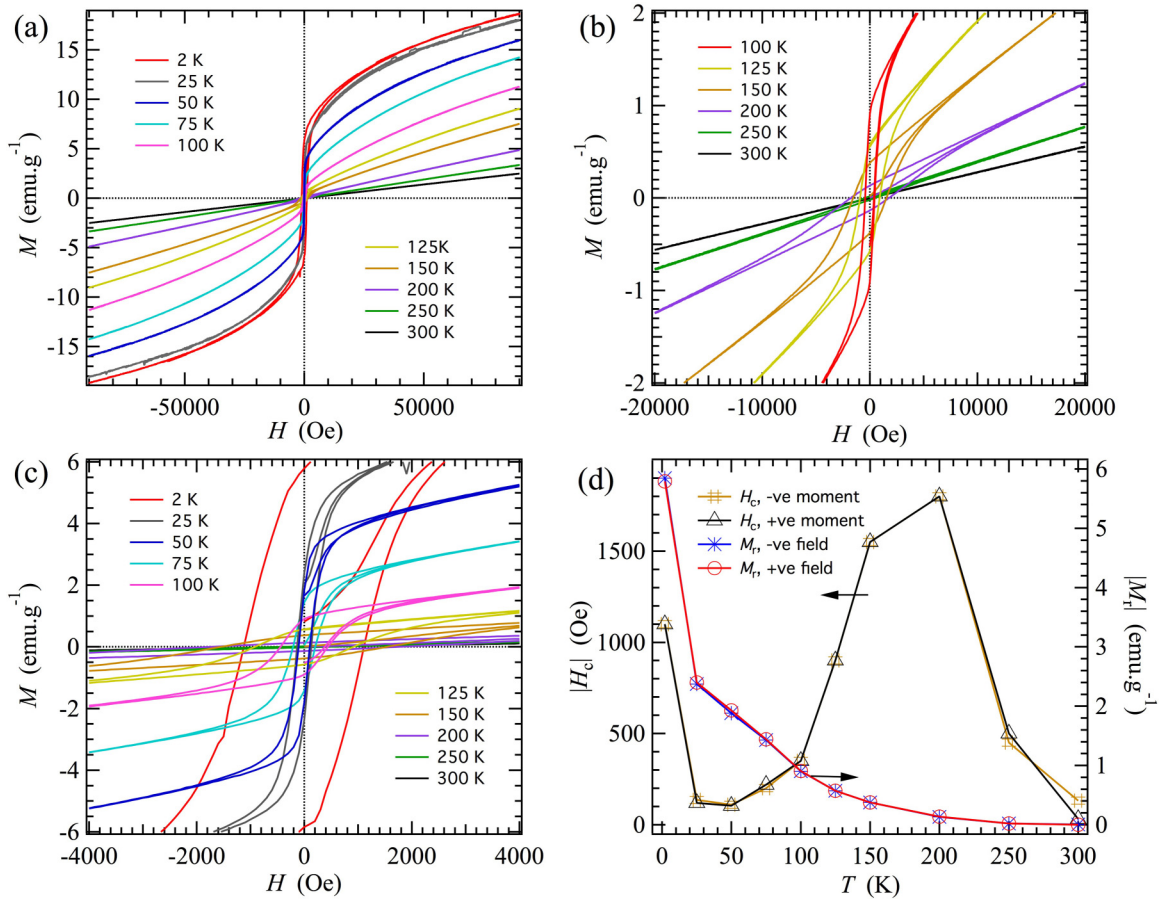
FIG. 4. (a) Isothermal magnetization (M) vs magnetic field (H) curves collected at ten different temperatures between 2 and 300 K, using the sample used for RUS with mass 0.0114 g. (b) Expanded view of the low-field region, showing open loops in the high-temperature range. (c) Expanded view showing open loops in the low-temperature range. (d) Variations with temperature of coercivity (H_c) and remanence (M_r) extracted from the M-H loops. Positive and negative values have been superimposed by multiplying the negative values by -1 and are within experimental uncertainty of being the same. M_r increases monotonically with falling temperature while H_c has a maximum at $\sim$150$-$200 K and a minimum at $\sim$50 K.

and a second linear segment between $\sim$235 and $\sim$265 K. The black dotted line depicts a fit for the Curie-Weiss expression, $\chi^{-1} = (T - \Theta)/C$, where C is the Curie constant and Θ is the Curie temperature, and gives $1/C = 95.5$ Oeg emu^{-1} K^{-1}, $\Theta = -35$ K. The effective paramagnetic moment obtained from $\mu_{\text{eff}} = 2.828\sqrt{C}$ is $6.4\,\mu_B$/f.u. If Mn^{3+} ($S = 2$) and Fe^{3+} (high spin, $S = 5/2$) are present, the spin only magnetic moment, μ_{SO}, is expected to be $(\mu_{\text{Mn}}^2 + \mu_{\text{Fe}}^2)^{1/2} = 7.68\,\mu_B$, where $\mu = [4S(S + 1)]^{1/2}$. The value obtained by Palakkal *et al.* [43] from their high-temperature data was $6.5\,\mu_B$/f.u. Previously reported values of Θ vary between $\sim$20 and $\sim$160 K [38,41,43,44,47,49]. The ZFC and FC data for 100 Oe above $\sim$300 K vary widely, indicating nonlinearity of the susceptibility at small fields in the stability field of the supposedly paramagnetic phase. It is not clear from the present paper whether this is due to the presence of a magnetic impurity or it is intrinsic to LFMO. A Curie-Weiss line has also been fit to the data in the interval $\sim$225$-$280 K, giving $1/C = 337$ Oe g emu^{-1} K^{-1} and $\Theta = 207$ K.

The derivative dM/dT has a broad, rounded minimum at $\sim$55 K for both the 1000-Oe ZFC and FC data sets [Fig. 1(c)], corresponding to the temperature at which the rate of increase of magnetization with falling temperature is greatest. dM/dT

for the ZFC data measured in a 100-Oe field shows two narrower minima, at $\sim$47 and $\sim$77 K, and there is a single minimum at $\sim$54 K from the FC data.

Isothermal magnetization ($M$$-$$H$) curves measured in the range $+70$ to -70 kOe at ten temperatures between 2 and 300 K are shown in Fig. 4(a). As indicated by the magnetization vs temperature data and as also found in previous studies (e.g., Bhame *et al.* [49], de Lima *et al.* [47], Palakkal *et al.* [43], Li *et al.* [44]), there is no evidence for a discrete magnetic phase transition, while opening of the curves at low fields [Fig. 4(b)] reveals the development of a ferromagnetic component. There is even a very small loop opening at 300 K, where paramagnetic behavior was expected. At 2 K the values of remanent magnetization, M_r, and coercivity, H_c, are $\sim$6 emu g^{-1} and $\sim$1.1 kOe, respectively. These are broadly similar to values found for other samples of LFMO annealed at high temperatures (e.g., Bhame *et al.* [49], de Lima *et al.* [47], Palakkal *et al.* [43], Li *et al.* [44]). M_r increases monotonically with falling temperature, in the same manner as reported by Palakkal *et al.* [43], but the coercivity, H_c, has a maximum at $\sim$150$-$200 K and a minimum at $\sim$50 K [Fig. 4(d)] which is quite different from the monotonic increase shown in Fig. 3 of Palakkal *et al.* [43]. Within experimental uncertainty, the
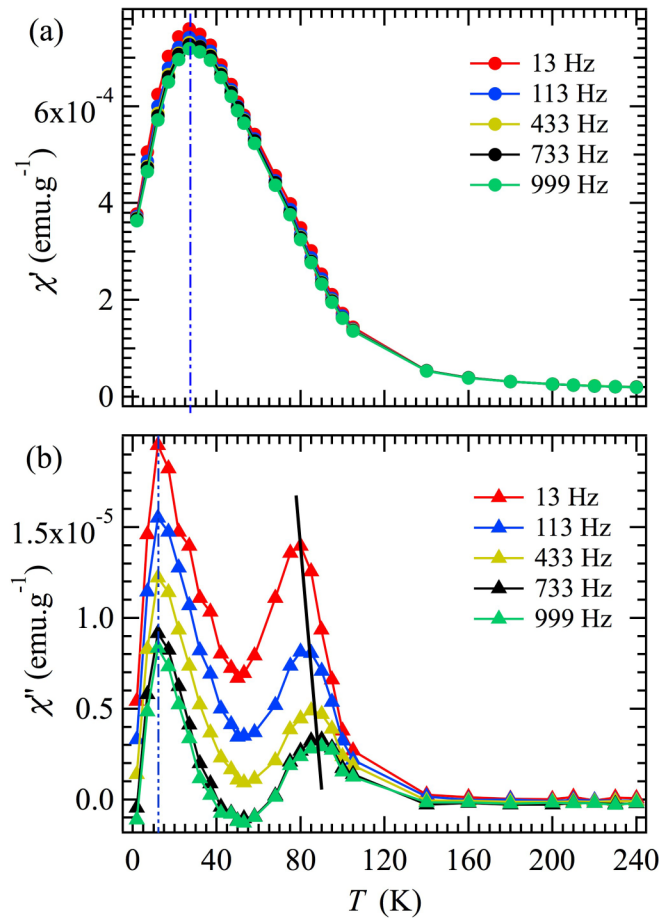
FIG. 5. (a) Real (χ') and (b) imaginary (χ') parts of ac susceptibility from 2 to 240 K, with external dc magnetic field $H = 30$ Oe and an ac magnetic field of 1 Oe, from a sample with mass 0.0774 g. The temperatures of the peak in χ' near 27 K and the peak in χ'' near 12 K do not change with frequency (blue broken lines). The black line shows how the temperature of the peak near 80 K increases with increasing frequency ($\sim$80 K at 13 Hz, $\sim$90 K at 999 Hz).

magnitudes of both H_c and M_r are symmetrical with respect to changing sign, signifying the absence of any overt exchange bias.

D. Ac magnetism

Figures 5(a) and 5(b) show the ac magnetic susceptibility of LFMO through the temperature interval 2–240 K, as measured using the sample with mass 0.0774 g at frequencies of 13, 113, 433, 733, and 999 Hz, with an external dc field of 30 Oe and an ac field amplitude of 1 Oe. There is a broad peak at $\sim$27 K in the real part, χ', of the ac susceptibility [Fig. 5(a)] and two peaks at $\sim$12 and $\sim$80−90 K in the imaginary part, χ'' [Fig. 5(b)]. The temperatures of the peak in χ' and the low-temperature peak in χ'' do not have any overt frequency dependence at the level of resolution of the data, but both have a trend of reducing maximum values with increasing frequency. The temperature of the peak in χ'' increases with increasing measuring frequency, $\sim$80 K at 13 Hz and $\sim$90 K at 999 Hz, consistent with some thermally activated loss process.

The same pattern was observed in the second set of measurements on the RUS sample (mass 0.0114 g, dc field = 20 Oe, ac field = 3 Oe), though the peaks in χ'' were not easy to discern because of poorer resolution. The derivative $d\chi'/dT$, of the data collected at 1 kHz, although also noisy, had a clear minimum at $\sim$74 K and perhaps another below $\sim$50 K, with similar overall form to the variation of dM/dT from the 100-Oe ZFC data shown in Fig. 1(c). No obvious anomalies were seen in either χ' or χ'' between 240 and 300 K.

There appear to be only two previous sets of ac data in the literature for comparison and these are different in detail. De *et al.* [41] observed a peak in χ' at $\sim$20 K, measured with ac fields of 2 and 4 Oe, and a very much smaller peak at $\sim$250 K. The amplitude of a single peak in χ'' was strongly frequency dependent but its temperature, $\sim$9 K, only weakly so. Palakkal *et al.* [45] reported only the imaginary part of the ac response for their sample which had a change in conductivity mechanism at $\sim$135 K. This showed two peaks. A peak near 225 K shifted to higher temperatures with increasing frequency and the slope from their Arrhenius plot of the data [their Fig. 7(b)] implies an activation energy of $\sim$0.44 eV for the loss process. In contrast, the amplitude of a peak near 85 K increased slightly with increasing frequency but its temperature was independent of frequency. The lower temperature limit of their data was 40 K but a trend increasing from below $\sim$50 K hints at the existence of an additional peak at lower temperatures. The most important common factor in all the data is that any changes in χ' accompanying changes in χ'' are small. This implies that the relaxational processes being detected do not have a strong influence on the total magnetization.

E. Elastic and anelastic properties

Segments of the primary RUS spectra collected during heating through the interval $\sim$95−298 K (Fig. 6) illustrate an increase in the resonance frequencies of all peaks with falling temperature, corresponding to stiffening of the shear modulus. A clear feature in the primary data is an increase of the stiffening trend below $\sim$160 K, accompanied by an interval of peak broadening. Although not shown in Fig. 6, a similar feature also occurs in the vicinity of $\sim$50 K.

Variations in f^2 and Q^{-1} from fitting of selected peaks in spectra collected in the heating sequence from $\sim$10 to $\sim$305 K are given in Fig. 7. The association of a small increase in f^2 beginning at $\sim$55 K with a peak in Q^{-1} near 45 K has a form that might be expected for a thermally activated Debye freezing process, and the loss peak can be fit on this basis using the expression [7,35,54–58]

$$Q^{-1}(T) Q_m^{-1} \left[\cosh\left\{ \frac{E_a}{R r_2(\beta)} \left(\frac{1}{T} - \frac{1}{T_m} \right) \right\} \right]^{-1}. \quad (1)$$

R is the gas constant, Q_m^{-1} is the maximum value of the loss at temperature T_m, E_a is an activation energy, and $r_2(\beta)$ relates to the width of a Gaussian spread of relaxation times. The parameter β represents the width of the Gaussian distribution, as illustrated by Nowick and Berry [59]; $\beta = 0$ and $r_2(\beta) = 1$ for a single relaxation time. The fit shown in Fig. 7 included a
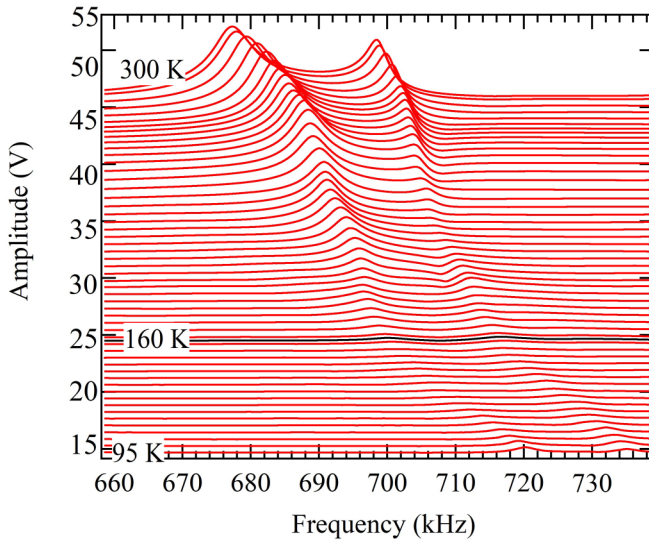
FIG. 6. Segments of RUS spectra collected during heating of a rectangular parallelepiped of LFMO with mass 0.0114 g. Each spectrum has been offset up the y axis in proportion to the temperature at which it was collected from ∼95 K to room temperature. The black line draws attention to a change in the trend of frequency variation with temperature at ∼160 K, with an interval of peak broadening just below this.

linear baseline and gave $E_a = 0.029(3)$ eV, $T_m = 44.2(8)$ K, and $Q_m^{-1} = 0.0057(5)$ at 725 kHz, with $r_2(\beta)$ fixed at 1.

The break in slope at ∼160 K seen in the primary spectra (Fig. 6) and in f^2 (Fig. 7) is also accompanied by an increase in acoustic loss but the data for Q^{-1} are rather noisy. The
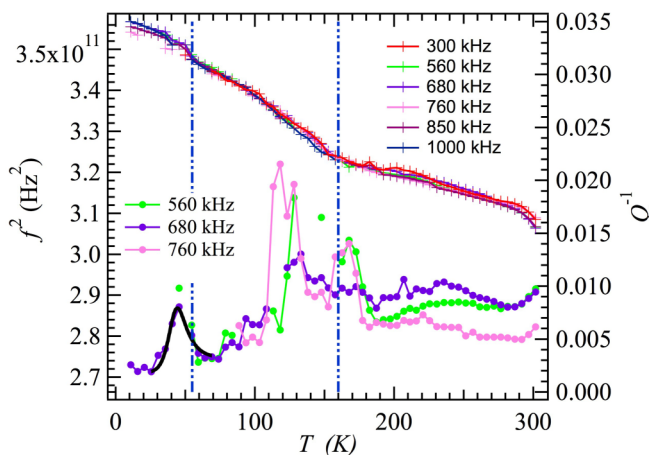
FIG. 7. Temperature dependence of f^2 for selected resonances, with scaling factors applied to each so that the values overlap near room temperature. Also shown are Q^{-1} values for the same resonances. Labels give the approximate frequency of each resonance near room temperature. The black solid curve near 45 K is a fit of Eq. (1) to Q^{-1} data for the resonance with frequency near 680 kHz. Q^{-1} data at higher temperatures are noisy and can be taken only to indicate that acoustic loss remains high from ∼120 K up to room temperature, though there is probably a peak in the loss below ∼150 K. Vertical dashed lines mark the temperatures at which there is a break in slope of f^2 (∼55 and ∼160 K).
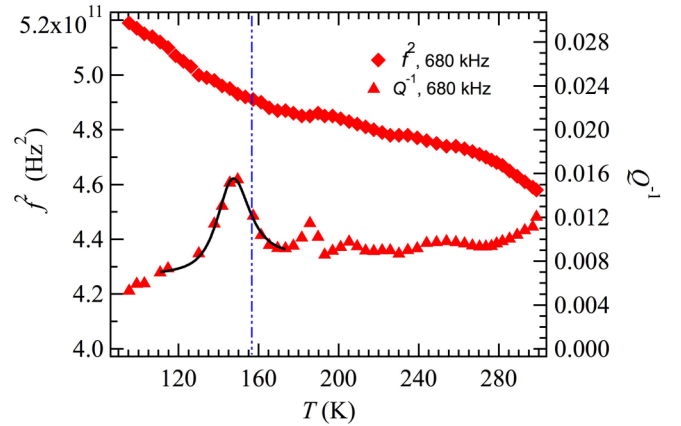
FIG. 8. f^2 and Q^{-1} data for a resonance peak with frequency near 680 kHz, which showed the peak in Q^{-1} at ∼145 K most clearly. The black solid curve is a fit of Eq. (1) to a segment of the Q^{-1} data, including a linear baseline.

form of the loss peak was more clear in the separate run from ∼95 to ∼300 K, as shown in Fig. 8 for a resonance peak with frequency near 680 kHz from the separate heating sequence. The fit of Eq. (1) to the peak in Q^{-1}, again with a linear baseline, gave $E_a = 0.27(1)$ eV, $T_m = 147.4(3)$ K, and $Q_m^{-1} = 0.0077(2)$ at ∼703.6 kHz. The value of $r_2(\beta)$ was fixed at 1.

V. DISCUSSION

Although there are differences in detail with respect to the magnetic properties of LFMO synthesized under different conditions, the general features of the material produced for the present paper remain the same. First, subject to the usual caveat that some samples may contain magnetic impurities, LFMO appears to be paramagnetic at high temperatures. Second, there is no evidence for any discrete magnetic ordering transitions. Third, the magnetic structures which become stable below room temperature develop in two stages, each with evidence of glassy character. The new RUS results reveal a significant role of strain coupling but it is far from clear how the elastic and anelastic anomalies relate to the magnetic behavior. Four possibilities may be considered: the elastic anomalies are related to the ferroelastic character of LFMO which is due to octahedral tilting at some high temperature from a parent cubic structure, there is some influence from local Jahn-Teller distortions even though the long-ranging cooperative effect is suppressed, there is some strain relaxation associated with hopping of electrons between cations, and/or there are magnetoelastic effects from more straightforward spin-lattice coupling.

A. Ferroelastic strain and twinning

Changes in elastic properties are invariably related to changes in strain, and it is well understood that spontaneous strains associated with phase transitions give characteristic patterns of elastic stiffening or softening and acoustic loss. Formally, the spontaneous strain accompanying a phase transition is a second rank tensor, with components e_1 to e_6,
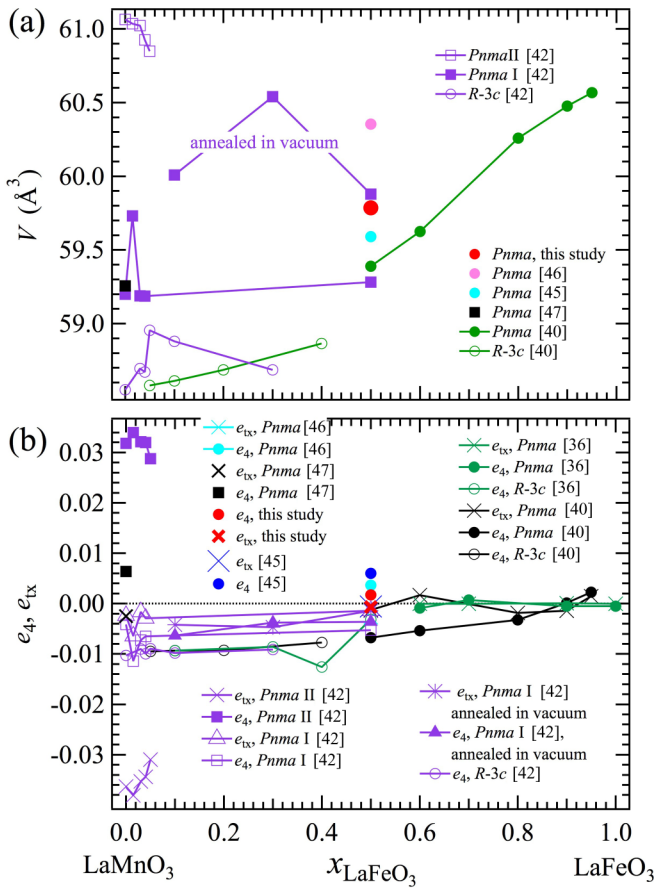
FIG. 9. (a) Unit-cell volume data at room temperature, taken from the literature. Sedykh *et al.* (2009) produced three different structure types with $x \leqslant 0.5$: *Pnma* II had been annealed in vacuum at 650–700 °C, *Pnma* I had been annealed at 850 °C, and the $R\bar{3}c$ phase had been annealed at 1100 °C. (b) Shear strains calculated using lattice parameter data from the literature.

which can be expressed in terms of a volume strain and symmetry-adapted shear strains [60]. Values of the volume, V, per formula unit of $La(Mn_{1-x}Fe_x)O_3$ at room temperature taken from the literature are reproduced in Fig. 9(a). Values for the shear strains $e_{tx}[= (1/\sqrt{3})(2e_1-e_2-e_3)]$ and e_4 were calculated using expressions for product structures in space groups $R\bar{3}c$ and *Pnma*, using expressions given in Zhang *et al.* [61], and are shown in Fig. 9(b). The parent state was taken as the cubic structure ($pm\bar{3}m$) with $a_o = V^{1/3}$ as an approximation for the reference lattice parameter. e_1-e_2, e_5, and e_6 are strictly zero in the orthorhombic structure, and $e_{tx} = e_1-e_2 = 0$, $e_4 = e_5 = e_6 \neq 0$ in the $R\bar{3}c$ structure.

Samples with low Fe contents annealed at 650–700 °C in vacuum have space group *Pnma*, the largest volume per formula unit, and shear strains of ∼3% at room temperature (Fig. 9), characteristic of the influence of a cooperative Jahn-Teller distortion in $LaMnO_3$ [62]. Synthesis in air and increasing Fe content cause values of both the volume and shear strains to reduce, indicating suppression of the Jahn-Teller contribution to the overall lattice distortion. Values of $|e_{tx}|$ and $|e_4|$ for $LaMn_{0.5}Mn_{0.5}O_3$ fall in the range ∼0−0.007, which is typical of the influence of octahedral tilting transitions, as seen, for example, in $BaCeO_3$ [61], $Pr_{0.48}Ca_{0.52}MnO_3$ [63],

and $SrZrO_3$ [64]. In a system without B-site ordering, e_4 arises from coupling with two order-parameter components, q_2 and q_4, related to the two octahedral tilt systems, and a Jahn-Teller order-parameter component, q_{JT}, according to [62,65]:

$$e_4 = \frac{-\lambda_5 q_4^2 - \lambda_{eM2+M3+q_{JT}q_2}}{C_{44}^{\circ}}. \qquad (2)$$

The coefficient λ_5 defines the strength of coupling between e_4 and q_4, as $\lambda_5 q_4^2$, and $\lambda_{eM2+M3+}$ defines the strength of coupling between e_4 and a combination of the second tilt component with the Jahn-Teller component as $\lambda_{eM2+M3+e_4q_{JT}q_2}$, which is a shear elastic constant of the cubic reference structure. If the only difference between LFMO samples was the octahedral tilt angle, e_4 would be expected to vary in magnitude but not in sign. What is observed instead for LFMO is a variation in both the magnitude and sign of e_4 [Fig. 9(b)], which implies $q_{JT} \neq 0$. The implication is that although the cooperative Jahn-Teller effect is greatly diminished by substitution of Fe^{3+} for Mn^{3+} [46,47] it is not completely suppressed. This, in turn, is consistent with the observation of Palakkal *et al.* [45] that the average B-site distortion increases with falling temperature.

The upper temperature limit for the *Pnma* structure of LFMO, with respect to the $R\bar{3}c$ structure or with respect to the parent cubic structure, is not yet known but it is unavoidable that crystals which grew below the transition point or had cooled through it would contain ferroelastic twins walls. Crystallization of $CaTiO_3$ within the stability field of the *Pnma* structure results in grains which contain twin domains on a scale of 0.5 μm, for example [66]. Twin walls due to octahedral tilting transitions in perovskites such as $SrTiO_3$ and $LaAlO_3$ are mobile under the influence of external stress at high temperatures, and their freezing or pinning by defects at low temperatures gives rise to a characteristic pattern of acoustic loss at RUS frequencies [51,67,68]. Typically, the pinning occurs above room temperature by a mechanism which involves oxygen vacancies, with an associated activation energy of ∼0.5−1 eV [69–71].

The closest analogy with LFMO for which RUS data are available is tetragonal Sr_2FeMoO_6, in which freezing/pinning of ferroelastic twin walls occurs at ∼340 K and has an associated activation energy of $\geqslant 0.65$ eV [7]. It is therefore unlikely that the pattern of acoustic loss below room temperature seen here in LFMO relates to the mobility of twin walls. On the other hand, the walls necessarily have a local structure which differs from that of the domains which they separate since they are, in effect, finite volumes containing strain gradients of e_4 and e_{tx} from ∼ + 0.002 to ∼ − 0.002 and ∼ − 0.001 to ∼ + 0.001, respectively. These will inevitably give rise to local variations in magnetic and electronic structure, enhancing any tendency there might be for heterogeneity in the local magnetic structure of a cluster or spin glass.

B. T^*/cluster glass/Griffiths-like phase

The linear relationship between moment and field at 300 K [Fig. 1(a)] demonstrates that the sample used in the present paper was close to, if not exactly, paramagnetic at room temperature. The Curie-Weiss fit to susceptibility data in the interval ∼330−400 K yields a negative Curie temperature of

~ -30 K, and the dip of magnetization below the Curie-Weiss line beginning at $T* \approx 330$ K [Fig. 1(b)] is also typical in form to what has been reported in the previous studies reviewed in Sec. II, above. A narrow temperature interval of linear susceptibility below T^* and the divergence of FC from ZFC magnetization are similar in form, if not in detail, to the previous reports which referred to the development of glassy magnetic structures at low temperatures. The additional information provided here is that these changes are not accompanied by any overt anomalies in ac magnetic properties measured in the frequency range $\sim 0.1 - 10$ kHz or in elastic/anelastic properties measured in the frequency range $\sim 0.2 - 1000$ kHz. The nature of the transition at $\sim T^*$ and the resulting glassy state are not yet fully characterized but if, as proposed by De *et al.* [41], for example, a superparamagnetic-type state containing weakly interacting locally ferromagnetic clusters develops, the dynamical spin ordering processes and any accompanying strain relaxation must be outside these frequencies ranges.

C. Charge transfer between cations

The resistance data in Fig. 3 show no evidence for the charge localization transition reported by Palakkal *et al.* [45] as occurring near 135 K, and Fig. 5(b) shows no sign of the large peak in χ'' reported at ~ 220 K for their sample. It is therefore assumed that the sample used in the present paper contained only Fe^{3+} and Mn^{3+}. However, the fit of Eq. (1) to the peak in Q^{-1} at ~ 150 K (Fig. 8) gave $E_a/r_2(\beta) = 0.27$ eV, which is close to the activation energy of 0.18 eV obtained from the resistance data. In addition, the acoustic loss peak measured at ~ 680 kHz in the present paper occurs at almost the same temperature as a dielectric loss peak observed between ~ 140 K (at 10 kHz) and ~ 210 K (at 1 MHz) from a sample of La_2NiMnO_6 [72]. The frequency dependence of the dielectric loss yielded an activation energy of 0.16 eV and the loss mechanism was attributed to asymmetric hopping of charge carriers between Ni^{2+} and Mn^{4+} in an electric field. If the acoustic loss was also due to freezing of a charge-transfer mechanism with an associated strain cloud, the Debye loss peak would be expected to be accompanied by a small increase in the shear modulus of the sample through the same temperature interval as the changes in Q^{-1}. This is not what is observed, in that there is instead a break in slope at ~ 160 K, followed by a steady increase in f^2 by up to $\sim 9\%$. A charge-transfer mechanism for the acoustic loss can probably be discounted, therefore.

D. Spin-glass transition and magnetoelastic coupling at low temperatures

In contrast with changes in properties at and below T^*, there are significant changes in the temperature dependence of magnetization, coercivity, ac magnetism, shear modulus ($\sim f^2$), and acoustic loss in the temperature range $\sim 2 - 150$ K [Figs. 1, 4(d), 5, and 7]. The expectation for a spin-glass transition is that there will be a maximum in χ'' at temperatures T_{max}, where relaxation times, τ_{max}, given by the condition $\omega\tau = 0$ will conform to Vogel-Fulcher dynamics as $\tau_{max} = \tau_0 \exp\{E_a/[R(T_{max} - T_{VF})]\}$ (e.g., De *et al.* [41]). The
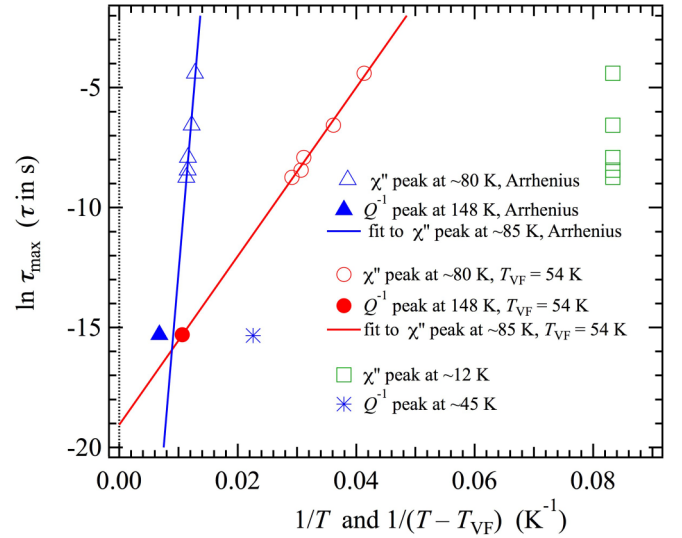
FIG. 10. Arrhenius and Vogel-Fulcher plots of data for relaxation times from maxima in χ'' and Q^{-1}, corresponding to the temperatures at which $\omega\tau = 0$. The blue line is a fit to data for the peak in χ'' near 80 K in Arrhenius form, but its extrapolation does not pass through the data point for Q^{-1}. The red line is a fit to data for χ'' in Vogel-Fulcher form with $T_{VF} = 54$ K, and this extrapolates through the point from the peak in Q^{-1} at 148 K. χ'' values from the peak near 12 K are not obviously related to the other data and neither is the data point from the peak in Q^{-1} near 45 K.

angular frequency, ω, is related to the measuring frequency, f, as $\omega = 2\pi f$, τ_0 is a constant, and E_a is an activation energy. T_{VF} is, in effect, the freezing point at zero frequency. If the acoustic loss peak at ~ 147 K and the peaks in χ'' near 85 K arise from the same relaxation, it should be possible to find a value for T_{VF} which gives all the relaxation times lying on a single straight line in a plot of $\ln \tau_{max}$ vs $1/(T - T_{VF})$. Figure 10 shows that τ_{max} values from χ'' and Q^{-1} lie on a single straight line if T_{VF} is set at $54\pm \sim 1$ K. This has a slope corresponding to $E_a/R = 352 \pm 21$ K and intercept $\ln \tau_0 = -19.1 \pm 0.7$ ($\tau_0 \sim 5 \times 10^{-9}$ s). Also shown in Fig. 10 are the data plotted in Arrhenius form, $\tau_{max} = \tau_0 \exp\lfloor E_a/RT_{max}\rfloor$, but the straight line fit to the data for χ'' ($E_a \sim 0.25$ eV, $\tau_0 \sim 65 \times 10^{-19}$ s) does not pass through the data point for Q^{-1}. A frequency dependent spin-glass transition is also probably a better explanation for the stiffening of f^2 below ~ 160 K, with the amount of stiffening scaling with the square of the order parameter, Q_g^2, due to coupling with shear strains, e_{sh}, of the form $\lambda e_{sh}^2 Q_g^2$. Quite independently, a criterion for identifying the low-temperature spin-glass transition is provided by the derivative, dM/dT [43], and data for the present sample put this at ~ 55 K when measured in a 1000-Oe field.

The small increase in f^2 at ~ 45 K, corresponding to stiffening of the shear modulus by $\sim 1\%$, accompanied by the peak in Q^{-1} have the typical form for Debye freezing of some defect which is coupled with strain. If the zero-frequency freezing point for the spin glass is ~ 54 K, it is possible that this relates to freezing of boundary regions between ferromagneticlike glassy domains. The additional peak in χ'' at ~ 12 K does not appear to be obviously related to this, based on their relative positions in Fig. 10, and presumably arises

from freezing of some other aspect of the microstructure of the spin glass. Freezing behavior at these low temperatures could also be associated with frustration of local Jahn-Teller distortions in a material which already has a spin-glass/spin-cluster structure due to frustration of spin states.

Values of E_a near ~ 0.03 eV extracted from both the Vogel-Fulcher fit and the acoustic loss peak at ~ 45 K are interpreted in terms of magnetoelastic relaxation dynamics involving coupling with local shear strains. They are comparable with values of $\geqslant \sim 0.07$ eV ($\tau_o \sim 10^{-11}$ s) and ~ 0.05 eV ($\tau_o \sim 10^{-14}$ s), respectively, for acoustic loss processes associated with charge order or orbital order in $Pr_{0.48}Ca_{0.52}MnO_3$ and helical magnetism in Cu_2SeO_3 below ~ 100 K [73,74]. The activation energy of ~ 0.08 eV ($\tau_o \sim 10^{-13}$ s) for an acoustic loss process in $YBa_2Cu_3O_{6+x}$ at $\sim 40-60$ K has been attributed to the movement under stress of polarons [75].

In LFMO the constraining dynamics of strain clouds coupled with spin configurations are most likely due to local changes in electronic structure, i.e., as changes in local Jahn-Teller distortions. Straightforward spin-lattice coupling would give a uniform change in shear strain, but a more likely mechanism is that there is coupling between spin state and electronic structure such that there are small changes in distortion of the average BO_6 octahedra. These would introduce a macroscopic shear strain and could, additionally, change the octahedral tilt angle.

E. Glassy magnetic structure

In terms of parameters which are commonly used to distinguish between spin-glass and cluster-glass behavior, the data for LFMO presented here give $(E_a/R)/T_{VF} \approx 6$, $(T_f - T_{VF})/T_{VF} \approx 0.5$ (where T_f is the freezing temperature given by the peak in χ''), and τ_o from the Vogel-Fulcher fit is $\sim 10^{-9}$ s. Following the discussion in Kumar *et al.* [76] for the glassy magnetic behavior of $NdCo_{1-x}Ni_xO_3$ ($x = 0.3-0.5$), these values are consistent with spin clusters, rather than canonical spin glass, with intercluster interactions giving rise to the glasslike freezing. In particular, the value of τ_o expected for a canonical spin-glass system is $\sim 10^{-12}-10^{-14}$ s and for a cluster glass the value of τ_o is expected to be $\sim 10^{-7}-10^{-10}$ s, as set out in the discussion of Sahoo *et al.* [77] for $La_{1.5}Ca_{0.5}CoMnO_6$. A further indicator of cluster-glass behavior is that the amplitudes of the peaks in χ'' decrease with increasing frequency [Fig. 5(b)], in contradiction with what is expected for a canonical spin glass [78].

The uniform increase in remanent magnetization, beginning at least by ~ 300 K [M_r in Fig. 4(d)], implies that the clusters contain a proportion of individual moments with a preferred ferromagnetic alignment that increases with falling temperature. There is no evidence in Fig. 4(d) for an exchange bias that could indicate the presence of interfaces between two phases with different states of magnetic order [79]. The steepest change in M_r occurs below ~ 25 K and is presumably related to the peak in χ'' at ~ 12 K [Fig. 5(b)]. The coercivity has a quite different pattern [H_c in Fig. 4(d) which is presumed to provide information on the ease with which boundaries between ferromagnetic clusters can move. The uniform increase in H_c below ~ 270 K would be expected for the movement of boundaries between magnetic clusters which

become progressively more ordered. Low values of H_c in the temperature interval $\sim 25-100$ K then indicate that resistance to displacements of these boundaries reduces steeply as glassy freezing of the clusters starts to become established.

Finer details, such as the double minimum in dM/dT measured at 100 Oe [Fig. 1(c)], are not understood but provide observations against which micromagnetic models can be tested. Detailed models of the magnetic behavior will need also to take account of the inevitable presence of ferroelastic twin walls and the likelihood that these will have different local configurations of spin states through their mutual dependence on strain relaxation.

VI. CONCLUSIONS

While details of the two glassy magnetic transitions below room temperature in LFMO are still not fully understood, it is now clear that they differ significantly in the extent to which they couple with shear strain. The transition from a paramagnetic state to a spin-glass/spin-cluster state near 270 K appears to involve only spins without overt changes in elastic properties. In contrast, the second glassy transition includes a significant component of strain coupling. Magnetic and acoustic loss dynamics can be explained in terms of a single magnetoelastic relaxation mechanism if the spin-glass transition follows Vogel-Fulcher dynamics with a zero-frequency freezing temperature of ~ 54 K. The low activation energy barrier can be understood in terms of local spin-lattice coupling. Increases in shear modulus have been attributed to strain coupling arising from the effect of spin states on electronic structure and site distortions with or without additional changes in octahedral tilt angles.

The overall glassy magnetic behavior is the result of frustration which arises from disorder of the B-site cations, Fe^{3+} and Mn^{3+}, and this is a contributory factor also in the suppression of cooperative Jahn-Teller distortions arising from Mn^{3+}. The evidence of variations in macroscopic shear strains is that the suppression is not complete, however. The presence of shear strain gradients through ferroelastic twin walls should also give rise to significant variations in local properties, to the extent that bulk properties might appear to be coming from two coexisting magnetic structures. The density and distribution of ferroelastic twin walls have not yet been investigated but are likely to be contributory factors in relation to the rather large variations in properties observed in crystals prepared under different experimental conditions.

With respect to tuning of the glassy behavior, evidence of coupling with strains means that thin films should have properties which will depend on their fit with a substrate. Substrates which impose shear strains on the film should have the potential to determine the electronic structure within homogeneous domains and also to control the distribution of domain walls which have properties that are highly sensitive to the nature of the glassy states.

[1] K. I. Kobayashi, T. Kimura, H. Sawada, K. Terakura, and Y. Tokura, Nature (London) **395**, 677 (1998).

[2] H. L. Feng, M. Arai, Y. Matsushita, Y. Tsujimoto, Y. Guo, C. I. Sathish, X. Wang, Y.-H. Yuan, M. Tanaka, and K. Yamaura, J. Am. Chem. Soc. **136**, 3326 (2014).

[3] M. I. Katsnelson, V. Y. Irkhin, L. Chioncel, A. I. Lichtenstein, and R. A. de Groot, Rev. Mod. Phys. **80**, 315 (2008).

[4] W. Eerenstein, N. D. Mathur, and J. F. Scott, Nature (London) **442**, 759 (2006).

[5] M. Imada, A. Fujimori, and Y. Tokura, Rev. Mod. Phys. **70**, 1039 (1998).

[6] H. Chen and A. Millis, Phys. Rev. B **93**, 104111 (2016).

[7] D. Yang, R. J. Harrison, J. A. Schiemer, G. I. Lampronti, X. Liu, F. Zhang, H. Ding, Y. G. Liu, and M. A. Carpenter, Phys. Rev. B **93**, 024101 (2016).

[8] N. S. Rogado, J. Li, A. W. Sleight, and M. A. Subramanian, Adv. Mater. **17**, 2225 (2005).

[9] M. Hashisaka, D. Kan, A. Masuno, M. Takano, Y. Shimakawa, T. Terashima, and K. Mibu, Appl. Phys. Lett. **89**, 032504 (2006).

[10] M. P. Singh, C. Grygiel, W. C. Sheets, P. Boullay, M. Hervieu, W. Prellier, B. Mercey, C. Simon, and B. Raveau, Appl. Phys. Lett. **91**, 012503 (2007).

[11] S. Q. Wu, S. Cheng, L. Lu, M. Liu, X. W. Jin, S. D. Cheng, and S. B. Mi, Sci. Rep. **8**, 2516 (2018).

[12] S. Pal, G. Sharada, M. Goyal, S. Mukherjee, B. Pal, R. Saha, A. Sundaresan, S. Jana, O. Karis, J. W. Freeland, and D. D. Sarma, Phys. Rev. B **97**, 165137 (2018).

[13] M. Sariful Sheikh, D. Ghosh, A. Dutta, S. Bhattacharyya, and T. P. Sinha, Mater. Sci. and Eng. B **226**, 10 (2017).

[14] M. P. Reddy, R. A. Shakoor, and A. M. A. Mohamed, Mater. Chem. Phys. **177**, 346 (2016).

[15] R. Masrour and A. Jabar, Chin. Phys. B **25**, 087502 (2016).

[16] X. W. Jin, L. Lu, S. B. Mi, M. Liu, and C. L. Jia, Appl. Phys. Lett. **109**, 031904 (2016).

[17] R. Takahashi, I. Ohkubo, K. Yamauchi, M. Kitamura, Y. Sakurai, M. Oshima, T. Oguchi, Y. Cho, and M. Lippmaa, Phys. Rev. B **91**, 134107 (2015).

[18] C. Li, B. Liu, Y. He, C. Lv, H. He, and Y. Xu, J. Alloys Compd. **590**, 541 (2014).

[19] P. Kumar, S. Ghara, B. Rajeswaran, D. Muthu, A. Sundaresan, and A. Sood, Solid State Commun. **184**, 47 (2014).

[20] A. K. Biswal, J. Ray, P. D. Babu, V. Siruguri, and P. N. Vishwakarma, J. Appl. Phys. **115**, 194106 (2014).

[21] Y. Guo, L. Shi, S. Zhou, J. Zhao, and W. Liu, Appl. Phys. Lett. **102**, 222401 (2013).

[22] D. Yang, W. Wang, T. Yang, G. I. Lampronti, H. Ye, L. Wu, Q. Yu, and S. Lu, APL Materials **6**, 066102 (2018).

[23] R. I. Dass and J. B. Goodenough, Phys. Rev. B **67**, 014401 (2003).

[24] M. N. Iliev, M. V. Abrashev, A. P. Litvinchuk, V. G. Hadjiev, H. Guo, and A. Gupta, Phys. Rev. B **75**, 104118 (2007).

[25] M. P. Singh, K. D. Truong, and P. Fournier, Appl. Phys. Lett. **91**, 042504 (2007).

[26] R. Galceran, L. López-Mir, B. Bozzo, J. Cisneros-Fernández, J. Santiso, L. Balcells, C. Frontera, and B. Martínez, Phys. Rev. B **93**, 144417 (2016).

[27] R. X. Silva, R. L. Moreira, R. M. Almeida, R. Paniago, and C. W. A. Paschoal, J. Appl. Phys. **117**, 214105 (2015).

[28] B. Orayech, I. Urcelay-Olabarria, G. A. Lopez, O. Fabelo, A. Faik, and J. M. Igartua, Dalton Trans. **44**, 13867 (2015).

[29] F. N. Sayed, S. N. Achary, S. K. Deshpande, B. Rajeswari, R. M. Kadam, S. Dwebedi, A. K. Nigam, and A. K. Tyagi, Z. Anorg. Allg. Chem. **640**, 1907 (2014).

[30] R. Galceran, C. Frontera, L. Balcells, J. Cisneros-Fernández, L. López-Mir, J. Roqueta, J. Santiso, N. Bagués, B. Bozzo, A. Pomar, F. Sandiumenge, and B. Martínez, Appl. Phys. Lett. **105**, 242401 (2014).

[31] J. Krishna Murthy and A. Venimadhav, J. Appl. Phys. **113**, 163906 (2013).

[32] Y. Qian, H. Wu, E. Kan, J. Lu, R. Lu, Y. Liu, W. Tan, C. Xiao, and K. Deng, J. Appl. Phys. **114**, 063713 (2013).

[33] K. Yoshimatsu, K. Nogami, K. Watarai, K. Horiba, H. Kumigashira, O. Sakata, T. Oshima, and A. Ohtomo, Phys. Rev. B **91**, 054421 (2015).

[34] R. Dass, J.-Q. Yan, and J. Goodenough, Phys. Rev. B **68**, 064415 (2003).

[35] M. Carpenter, J. Phys.: Condens. Matter **27**, 263201 (2015).

[36] Y. Q. Jia, S. T. Liu, Y. Wu, M. Z. Jin, X. W. Liu, and M. L. Liu, Phys. Status Solidi A **143**, 15 (1994).

[37] V. L. Joseph Joly, S. D. Bhame, P. A. Joy, and S. K. Date, J. Magn. Magn. Mater. **261**, 433 (2003).

[38] K. De, R. Ray, R. Narayan Panda, S. Giri, H. Nakamura, and T. Kohara, J. Magn. Magn. Mater. **288**, 339 (2005).

[39] X.-D. Zhou, J. B. Yang, E.-C. Thomsen, Q. Cai, B. J. Scarfino, Z. Nie, G. W. Coffey, W. J. James, W. B. Yelon, H. U. Anderson, and L. R. Pedersona, J. Electrochem. Soc. **153**, J133 (2006).

[40] X.-D. Zhou, L. R. Pederson, Q. Cai, J. Yang, B. J. Scarfino, M. Kim, W. B. Yelon, W. J. James, H. U. Anderson, and C. Wang, J. Appl. Phys. **99**, 08M918 (2006).

[41] K. De, M. Thakur, A. Manna, and S. Giri, J. Appl. Phys. **99**, 013908 (2006).

[42] V. D. Sedykh, V. S. Shekhtman, A. V. Dubovitskǐ, I. I. Zver'kova, and V. I. Kulakov, Phys. Solid State **51**, 373 (2009).

[43] J. P. Palakkal, P. N. Lekshmi, S. Thomas, K. G. Suresh, and M. R. Varma, RSC Advances **5**, 105531 (2015).

[44] Q. Li, L. Xing, and M. Xu, J. Alloys Compd. **710**, 771 (2017).

[45] J. P. Palakkal, C. R. Sankar, A. P. Paulose, and M. R. Varma, J. Alloys Compd. **743**, 403 (2018).

[46] D. V. Karpinsky, I. O. Troyanchuk, and V. V. Sikolenko, J. Phys.: Condens. Matter **19**, 036220 (2007).

[47] O. F. de Lima, J. A. H. Coaquira, R. L. de Almeida, L. B. de Carvalho, and S. K. Malik, J. Appl. Phys. **105**, 013907 (2009).

[48] R. D. Shannon, Acta. Cryst. A **32**, 751 (1976).

[49] S. D. Bhame, V. L. J. Joly, and P. A. Joy, Phys. Rev. B **72**, 054426 (2005).

[50] A. Coelho, *TOPAS-Academic V6 software* (Coelho Software, Brisbane, Australia, 2007).

[51] A. Migliori, J. L. Sarrao, W. M. Visscher, T. M. Bell, M. Lei, Z. Fisk, and R. G. Leisure, Physica B: Condensed Matter **183**, 1 (1993).

[52] R. E. A. McKnight, M. A. Carpenter, T. W. Darling, A. Buckley, and P. A. Taylor, Am. Mineral. **92**, 1665 (2007).

[53] R. Schmidt, A. Basu, and A. W. Brinkman, Phys. Rev. B **72**, 115101 (2005).

[54] D. Yang, T. Chatterji, J. A. Schiemer, and M. A. Carpenter, Phys. Rev. B **93**, 144109 (2016).

[55] C. Salazar Mejía, N. O. Born, J. A. Schiemer, C. Felser, M. A. Carpenter, and M. Nicklas, Phys. Rev. B **97**, 094410 (2018).

[56] L. Zhang, X. Ren, and M. A. Carpenter, Phys. Rev. B **95**, 054116 (2017).

[57] L. Zhang, X. Lou, D. Wang, Y. Zhou, Y. Yang, M. Kuball, M. A. Carpenter, and X. Ren, Phys. Rev. Appl. **8**, 054018 (2017).

[58] M. A. Carpenter, J. A. Schiemer, I. Lascu, R. J. Harrison, A. Kumar, R. S. Katiyar, N. Ortega, D. A. Sanchez, C. S. Mejia, W. Schnelle, M. Echizen, H. Shinohara, A. J. F. Heap, R. Nagaratnam, S. E. Dutton, and J. F. Scott, J. Phys.: Condens. Matter **27**, 285901 (2015).

[59] A. Nowick and B. Berry, *Anelastic Relaxation in Crystalline Solids* (1945), Chap. 6, pp. 130–147.

[60] M. A. Carpenter, E. K. H. Salje, and A. Graemebarber, Eur. J. Mineral. **10**, 621 (1998).

[61] Z. Zhang, J. Koppensteiner, W. Schranz, J. B. Betts, A. Migliori, and M. A. Carpenter, Phys. Rev. B **82**, 014113 (2010).

[62] M. A. Carpenter and C. J. Howard, Acta Crystallogr., Sect. B **65**, 134 (2009).

[63] M. A. Carpenter, R. E. A. McKnight, C. J. Howard, and K. S. Knight, Phys. Rev. B **82**, 094101 (2010).

[64] E. A. M. Ruth, C. J. Howard, and M. A. Carpenter, J. Phys.: Condens. Matter **21**, 015901 (2009).

[65] M. A. Carpenter and C. J. Howard, Acta Crystallogr., Sect. B **65**, 147 (2009).

[66] S. Webb, I. Jackson, and J. Fitz Gerald, Phys. Earth Planet. Inter. **115**, 259 (1999).

[67] M. Carpenter, A. Buckley, P. Taylor, and T. Darling, J. Phys.: Condens. Matter **22**, 035405 (2010).

[68] J. F. Scott, J. Bryson, M. A. Carpenter, J. Herrero-Albillos, and M. Itoh, Phys. Rev. Lett. **106**, 105502 (2011).

[69] R. J. Harrison and S. A. T. Redfern, Phys. Earth Planet. Inter. **134**, 253 (2002).

[70] R. J. Harrison, S. A. Redfern, and J. Street, Am. Mineral. **88**, 574 (2003).

[71] R. J. Harrison, S. A. T. Redfern, and E. K. H. Salje, Phys. Rev. B **69**, 144101 (2004).

[72] D. Choudhury, P. Mandal, R. Mathieu, A. Hazarika, S. Rajan, A. Sundaresan, U. V. Waghmare, R. Knut, O. Karis, P. Nordblad, and D. D. Sarma, Phys. Rev. Lett. **108**, 127201 (2012).

[73] M. A. Carpenter, C. J. Howard, R. E. McKnight, A. Migliori, J. B. Betts, and V. R. Fanelli, Phys. Rev. B **82**, 134123 (2010).

[74] D. M. Evans, J. A. Schiemer, M. Schmidt, H. Wilhelm, and M. A. Carpenter, Phys. Rev. B **95**, 094426 (2017).

[75] G. Cannelli, R. Cantelli, F. Cordero, F. Trequattrini, and M. Ferretti, Phys. Rev. B **54**, 15537 (1996).

[76] V. Kumar, Y. Kumar, R. Kumar, D. K. Shukla, S. K. Arora, I. V. Shvets, and R. Kumar, J. Appl. Phys. **113**, 043918 (2013).

[77] R. C. Sahoo, S. K. Giri, D. Paladhi, A. Das, and T. K. Nath, J. Appl. Phys. **120**, 033906 (2016).

[78] T. Elovaara, H. Huhtinen, S. Majumdar, and P. Paturi, J. Phys.: Condens. Matter **26**, 266005 (2014).

[79] B. M. Wang, Y. Liu, P. Ren, B. Xia, K. B. Ruan, J. B. Yi, J. Ding, X. G. Li, and L. Wang, Phys. Rev. Lett. **106**, 077203 (2011).